Absorption effects on plasmon polariton-gap solitons in Kerr/metamaterial superlattices

2014 EPL 106 64001

(http://iopscience.iop.org/0295-5075/106/6/64001)

A Letters Journal Exploring the Frontiers of Physics

June 2014

EPL, **106** (2014) 64001
doi: 10.1209/0295-5075/106/64001

www.epljournal.org

Absorption effects on plasmon polariton-gap solitons in Kerr/metamaterial superlattices

E. Reyes-Gómez[1], S. B. Cavalcanti[2] and L. E. Oliveira[3]

[1] *Instituto de Física, Universidad de Antioquia UdeA - Calle 70 No. 52-21, Medellín, Colombia*
[2] *Instituto de Física, Universidade Federal de Alagoas - Maceió-AL, 57072-970, Brazil*
[3] *Instituto de Física, Universidade Estadual de Campinas (Unicamp) - Campinas-SP, 13083-859, Brazil*

received 18 April 2014; accepted in final form 22 May 2014
published online 16 June 2014

PACS 41.20.Jb – Electromagnetic wave propagation; radiowave propagation
PACS 42.70.Gi – Light-sensitive materials
PACS 42.70.Qs – Photonic bandgap materials

Abstract – A thorough study of the absorption effects on the plasmon polariton-gap soliton-induced transparency in 1D Kerr/metamaterial superlattices is presented. Results indicate that for frequencies close to the bottom or top edge of the bulk-like longitudinal plasmon-polariton gap, the transmission of a finite Kerr/metamaterial superlattice presents a multistable behavior, switching from very low values to the maximum transparency at particular values of the incident power even in the presence of loss effects. Moreover, calculations suggest the existence of resonant plasmon polariton-gap solitons of various orders depending on the particular value of the incident power. The present results reveal that plasmon polariton-gap soliton-induced resonant solutions lead to the transparency of a stack with nonlinear inclusions, a nonlinear optical analog of the electronic barrier-transmission resonances.

Over the past years the advent of metamaterials based on nanostructured metal/dielectric composites and exhibiting a negative index of refraction has provided a myriad of exciting phenomena such as invisibility and super-resolution imaging among many others [1,2]. Recently, the merging of plasmonic and metamaterial areas has opened up a new perspective towards achieving the ultimate control of light in the nanoscale dimension [3,4]. The collective excitation of charge and current densities by an incident electromagnetic radiation has led to localized plasmon resonances in one-dimensional (1D) superlattices composed of dieletric/metamaterial bilayers of both surface [5] and bulk-like longitudinal plasmon polaritons (PPs) [6,7]. Another field of interest concerns the excitation of solitons in plasmonic lattices. These so-called surface plasmonic lattice solitons have been reported recently in arrays of metallic nanowires embedded in a nonlinear medium [8], along the interface between homogeneous media and a 1D nonlinear plasmonic lattice [9]. Lately, vector plasmonic lattice solitons have also been reported in metal-dielectric waveguide arrays [10]. Nevertheless, these are all connected with surface PPs and as we shall see in the following we are interested in bulk plasmon solitons in the vicinity of bulk PP gaps. Substitution of dielectric layers by Kerr-type nonlinear ones in the dielectric/metamaterial bilayers described above has revealed a good deal of phenomena such as induced transparency, multistability [11–14] and the existence of localized PP solitons [15]. However, practical applications are significantly limited by the inherent and strong energy dissipation, which are inevitable in plasmonic metamaterial nanostructures, although significant effort has been devoted to obtain low-loss devices by optimizing structural geometries [16] and using gain materials [17]. Nevertheless, to properly evaluate the performance of the PP-gap soliton-induced transparency, in the present work we present a thorough study on the impact of absorption on the excitation of PP-gap solitons.

Let us begin by considering an heterostructure composed by bilayers AB comprising a Kerr medium (layer A) and a metamaterial (B), whose widths are a and b, respectively. Let the z-direction be the stacking direction of the superlattice and suppose that it is surrounded by vacuum. Layers A are characterized by magnetic permeability μ_A and electric permittivity given by

$$\epsilon_A = \epsilon_A^0 + \alpha |E(z)|^2, \tag{1}$$

where $E = E(z)$ is the electric-field amplitude of the electromagnetic field within the heterostructure. The slabs B

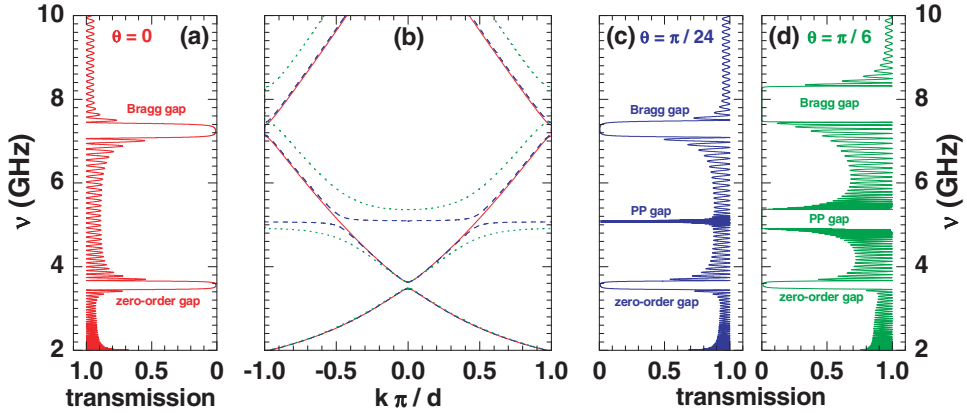

Fig. 1: (Color online) Transmission coefficient as a function of the wave frequency in a heterostructure composed of 32 AB bilayers, with $a = b = 10\,\text{mm}$, in the absence of absorption and nonlinearity ($\gamma = 0$ and $\alpha = 0$, respectively), for (a) normal and oblique incidence with (c) $\theta = \pi/24$ and (d) $\theta = \pi/6$. Panel (b) shows the dispersion relation corresponding to the infinite heterostructure for normal and oblique incidence with $\theta = \pi/24$ and $\theta = \pi/6$ (solid, dashed, and dotted lines, respectively). Results were obtained by setting $\epsilon_A = \epsilon_A^0 = 2$ and $\mu_A = 1$ in layers A, whereas the magnetic permeability and electric permitivitty of slabs B are given by eqs. (2) and (3), respectively. The oblique incidence was considered in the TE configuration.

are characterized by a dispersive and absorptive metamaterial with magnetic permeability and electric permittivity given by [13,14]

$$\mu_B = 1.0 + \frac{25}{0.814 - \nu^2 - i\nu\gamma} \tag{2}$$

and

$$\epsilon_B = 1.6 + \frac{40}{0.81 - \nu^2 - i\nu\gamma}, \tag{3}$$

respectively. Here ν is the linear frequency in GHz and γ is the damping constant which accounts for absorption within layers B. Choosing the transversal-electric (TE) configuration, the electric-field amplitude satisfies the differential equation

$$-\frac{\mathrm{d}}{\mathrm{d}z}\left[\frac{1}{\mu}\frac{\mathrm{d}}{\mathrm{d}z}E(z)\right] - \left[\frac{\omega^2}{c^2}\epsilon(z) - \frac{q^2}{\mu(z)}\right]E(z) = 0, \tag{4}$$

where $\omega = 2\pi\nu$, $q = \frac{\omega}{c}\sin\theta$ is the wave vector component in the x-direction, θ is the incidence angle relative to the vacuum, and $\epsilon(z)$ and $\mu(z)$ are the electric permittivity and magnetic permeability of the heterostructure which are given by $\epsilon_A\,(\epsilon_B)$ and $\mu_A\,(\mu_B)$, respectively, if z is in layer A (B). The electric-field amplitude may be computed by numerically solving eq. (4), by taking into account the continuity of both E and $\frac{1}{\mu}\frac{\mathrm{d}}{\mathrm{d}z}E$ at each interface. In addition, the reflection and transmission coefficients may be obtained by imposing boundary conditions at the vacuum regions, *i.e.*,

$$E(z) = \begin{cases} E_i e^{iQ_0 z} + E_r e^{-iQ_0 z}, & \text{if } z < 0, \\ E_t e^{iQ_0(z-L)}, & \text{if } z > L, \end{cases} \tag{5}$$

where $Q_0 = \frac{\omega}{c}\cos\theta$, L is the system length, E_i, E_r and E_t are the amplitudes of the incident, reflected and transmitted fields, respectively, and $z = 0$ at the beginning of the system. To compute [18–20] the reflection and transmission coefficients for a given value of ω, one may first assign a numerical value to the electric-field amplitude and its derivative at the outer interface. Then one successively computes the electric-field amplitude at each internal A and B layers, by taking into account the above-mentioned boundary conditions for both E and its derivative at each interface, until the first ($z = 0$) interface. Finally, one obtains E_i and E_r, and the transmission $T = \left|\frac{E_t}{E_i}\right|^2$ and reflection $R = \left|\frac{E_r}{E_i}\right|^2$ coefficients.

Let us begin by describing the linear nondissipative results, *i.e.*, the results obtained in the study of an heterostructure in the absence of disorder and absorption, when the parameters used in eqs. (1) to (3) are chosen as $\gamma = \alpha = 0$. In fig. 1, the transmission coefficient, in the TE configuration, is plotted as a function of the incoming wave frequency for normal (fig. 1(a)) and oblique incidence (figs. 1(c) and (d)) illustrating the null transmittance region around the ν_m^p bulk-like longitudinal magnetic plasmon frequency ($\mu_B = 0$ at $\nu_m^p = 5.0807\,\text{GHz}$). We have also plotted the dispersion for an infinite-layered system (fig. 1(b)), for it clearly anticipates the excitation of PP modes around the magnetic plasmon frequency. Note that the pure photon branch in the normal incidence case splits up into two branches, for oblique incidence, around the magnetic plasmon frequency, giving rise to the PP gap and consequently, to PP modes at both branches above and below the plasmon frequency. The physical origin of the PP gap stems from the fact that, in a TE configuration and for oblique incidence, there is a magnetic-field component in the stacking direction which couples to the bulk-like longitudinal magnetic plasmon mode [6]. It should be noted here that (cf. fig. 1(b)) for $\theta = \pi/24$ the edges of the PP gap occur at $\nu_- = 5.0663\,\text{GHz}$ and $\nu_+ = 5.0976\,\text{GHz}$,

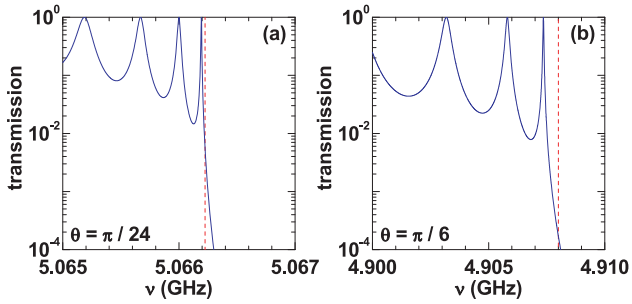

Fig. 2: (Color online) Transmission coefficient, corresponding to the TE configuration, as a function of the wave frequency for (a) $\theta = \pi/24$ and (b) $\theta = \pi/6$. Results were obtained for $\alpha = 0$ in eq. (1) and $\gamma = 0$ in eqs. (2) and (3), in the same heterostructure considered in fig. 1. The vertical dashed line in panel (a) ((b)) is located at $\nu = 5.0662$ GHz ($\nu = 4.9080$ GHz) in the vicinity of the lower edge of the TE PP gap displayed in fig. 1(c) (fig. 1(d)).

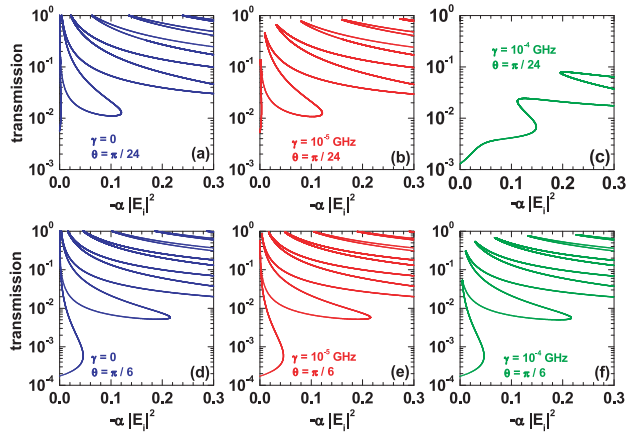

Fig. 3: (Color online) Transmission coefficient of the TE modes as a function of the defocusing nonlinearity power. The linear and geometrical parameters are the same as the ones used in fig. 1. Results were obtained for $\nu = 5.0662$ GHz ($\theta = \pi/24$) and $\nu = 4.9080$ GHz ($\theta = \pi/6$), in the vicinity of the bottom of the TE PP gap (cf. vertical dashed lines in fig. 2) depicted in figs. 1(c) and (d), respectively. Calculations were performed for $\gamma = 0$, $\gamma = 10^{-5}$ GHz, and $\gamma = 10^{-4}$ GHz.

whereas for $\theta = \pi/6$ it becomes wider occurring between $\nu_- = 4.9079$ GHz and $\nu_+ = 5.3612$ GHz. It is important to notice that the PP gap is 0.4533 GHz for $\theta = \pi/6$ whereas for $\theta = \pi/24$ it is much narrower (0.0313 GHz), as one would expect, considering that the magnetic-field component along the stacking direction is much larger for the latter than the former. This results in a much stronger coupling, for $\theta = \pi/6$, between the incident electromagnetic field and the longitudinal bulk-like magnetic plasmon mode. Furthermore, it is clear that the finite system (32 bilayers) transmission properties agree remarkably well with the results obtained in the vicinities of the PP gap, zero-n gap as well as the Bragg gap for the infinite photonic periodic superlattice.

Table 1: Positions ($-\alpha|E_i|^2$) of the first three peaks of the TE transmission coefficient as a function of the defocusing nonlinearity power (cf. figs. 3(a), (b), and (c)). Results were obtained for three different values of the damping constant γ, for oblique incidence with $\theta = \pi/24$ and $\nu = 5.0662$ GHz in the vicinity of the bottom edge of the TE PP gap depicted in fig. 1(c).

γ (GHz)	Peak 1	Peak 2	Peak 3
0	1.8199×10^{-4}	0.0044	0.0218
10^{-5}	0.0013	0.0095	0.0324
10^{-4}	–	0.1261	0.2015

Table 2: Positions ($-\alpha|E_i|^2$) of the first three peaks of the TE transmission coefficient as a function of the defocusing nonlinearity power (cf. figs. 3(d), (e), and (f)). Results were obtained for three different values of the damping constant γ, for oblique incidence with $\theta = \pi/6$ and $\nu = 4.908$ GHz in the vicinity of the bottom edge of the TE PP gap depicted in fig. 1(d).

γ (GHz)	Peak 1	Peak 2	Peak 3
0	2.4127×10^{-4}	0.0034	0.0159
10^{-5}	4.3021×10^{-4}	0.0039	0.0172
10^{-4}	0.0046	0.0109	0.0295

Let us now focus in the particular range in the vicinity of the lower-frequency edge of the magnetic PP gap around $\nu_m^p = 5.0807$ GHz to compare the TE transmission properties of the superlattice for $\theta = \pi/24$ and $\theta = \pi/6$ (cf. fig. 2), in the absence of loss and nonlinearity, *i.e.*, $\gamma = 0$ and $\alpha = 0$, respectively. The vertical dashed lines in fig. 2 essentially indicate the frequencies in the vicinity of the lower edge of the PP gap for which the transmission becomes negligibly small, *i.e.*, $\nu = 5.0662$ GHz for $\theta = \pi/24$ and $\nu = 4.9080$ GHz for $\theta = \pi/6$. Let us now include effects of nonlinearity and loss to study the transmission switching and multistability phenomena [15]. Figure 3 illustrates the transmission switch to one for various discrete values of the incident power, *i.e.*, the nonlinearity induces to several transparency peaks at specific field-intensity values as described in tables 1 and 2, in the particular cases of $\theta = \pi/24$ and $\theta = \pi/6$, respectively. We note that even in the presence of loss, results clearly show that higher values of the incident electromagnetic intensity lead to bistability and to a richer structure with increasing multistable output. Moreover, those particular states of total transparency correspond to PP-gap soliton-like localized solutions (see figs. 4 and 5) due to the resonant coupling between the incoming electromagnetic wave and plasmon modes of the metamaterial. Such hybrid modes lead to the transparency of the stack with nonlinear inclusions. Results clearly show that the induced transparency stems from the resonant excitation of one-soliton, two-soliton, ..., n-soliton solutions as depicted in fig. 4 ($\theta = \pi/24$) and fig. 5 ($\theta = \pi/6$) for various values of

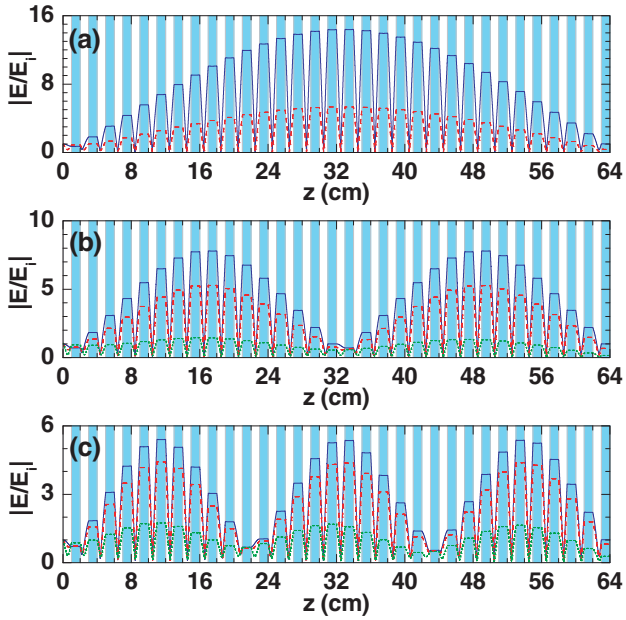

Fig. 4: (Color online) PP-gap solitons for oblique incidence with $\theta = \pi/24$ obtained for the system considered in fig. 1. Solid, dashed and dotted lines correspond to $\gamma = 0$, $\gamma = 10^{-5}$ GHz and $\gamma = 10^{-4}$ GHz, respectively. Results for each value of γ were obtained for the values of $-\alpha|E_i|^2$ corresponding to the three first local maxima of the transmission coefficient as a function of the defocusing nonlinearity power at $\nu = 5.0662$ GHz, as listed in table 1.

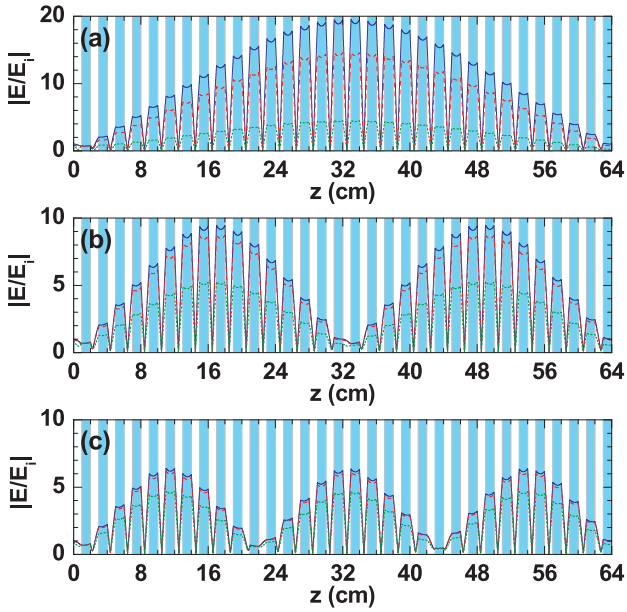

Fig. 5: (Color online) PP-gap solitons for oblique incidence with $\theta = \pi/6$ obtained for the system considered in fig. 1. Solid, dashed and dotted lines correspond to $\gamma = 0$, $\gamma = 10^{-5}$ GHz and $\gamma = 10^{-4}$ GHz, respectively. Results for each value of γ were obtained for the values of $-\alpha|E_i|^2$ corresponding to the three first local maxima of the transmission coefficient as a function of the defocusing nonlinearity power at $\nu = 4.908$ GHz, as listed in table 2.

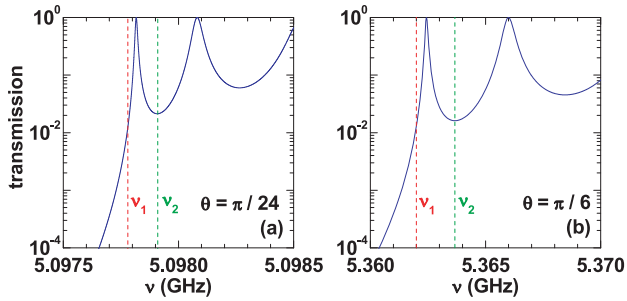

Fig. 6: (Color online) Transmission coefficient corresponding to the TE configuration as a function of the wave frequency for $\alpha = 0$ and $\gamma = 0$ in the structure considered in fig. 1, for (a) $\theta = \pi/24$ and (b) $\theta = \pi/6$. In panel (a) ((b)), vertical dashed lines at $\nu_1 = 5.09778$ GHz ($\nu_1 = 5.3620$ GHz) and $\nu_2 = 5.09791$ GHz ($\nu_2 = 5.3637$ GHz) are located in the vicinity of the top edge of the TE PP gap, depicted in fig. 1(c) (fig. 1(d)).

the damping parameter γ which phenomenologically describes absorptive losses. These results indicate that for high enough field intensities, even the higher-order soliton modes survive against relatively high losses. It should be noted here that, for $\theta = \pi/24$ and $\gamma = 10^{-4}$ GHz, there is no peak in the transmission associated to one-soliton excitation (cf. figs. 3(c) and 4(a)). This is due to the fact that loss effects are quite high and the magnetic-field component along the stacking direction is much smaller for $\theta = \pi/24$ as compared with $\theta = \pi/6$, resulting in a weak coupling, for $\theta = \pi/24$, between the incident electromagnetic field and the longitudinal bulk-like magnetic plasmon mode. Nevertheless, one finds, for example, two-soliton and three-soliton excitations (cf. figs. 4(b) and (c)) for the high $\gamma = 10^{-4}$ GHz loss as they occur for higher nonlinearity strength. As we have seen above, these results have been obtained for frequencies in the neighborhood of the lower edge of the bandgap. Let us then proceed and study the upper band edge neighborhood. To this end, we turn to fig. 6 which diplays results as in fig. 2 except for now, $\theta = \pi/6$ and we focus at the top edge of the TE PP gap. In particular, dashed vertical lines correspond to $\nu_1 = 5.3620$ GHz and $\nu_2 = 5.3637$ GHz, in the vicinity of the top edge of the TE PP gap displayed in fig. 1(d). The inclusion of nonlinearity and absorption is depicted in fig. 7 which shows transmission as a function of the nonlinearity. We find transmission switching to one and bistability for $\nu = 5.3637$ GHz in the presence of absorption, whereas for $\nu = 5.3620$ GHz no transmission switching is observed. Results in fig. 8 illustrate the induced transparency phenomenon corresponding to the local maxima of the transmission coefficient (cf. fig. 7 and tables 3 and 4) with the resonant excitation of a localized one-soliton solution even in the presence of absorption effects. As we have mentioned before, for $\theta = \pi/24$ and $\gamma = 10^{-4}$ GHz, the coupling between the incident electromagnetic field and the longitudinal bulk-like magnetic

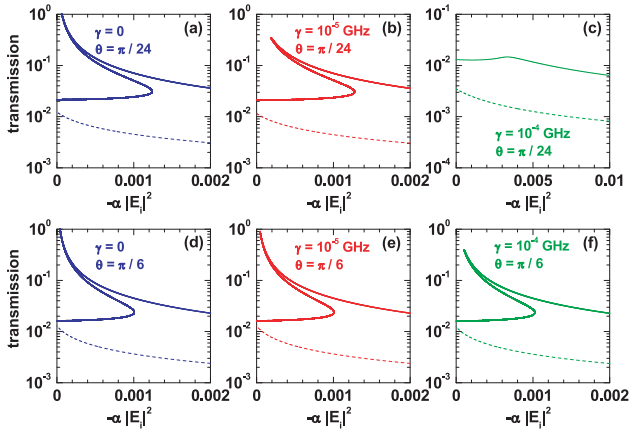

Fig. 7: (Color online) Transmission coefficient of the TE modes, as a function of the defocusing nonlinearity power, for three different values of the damping constant. Results were obtained for $\theta = \pi/24$ and $\theta = \pi/6$. Dashed and solid lines in panels (a), (b), and (c) ((d), (e), and (f)) correspond to $\nu_1 = 5.09778\,\mathrm{GHz}$ ($\nu_1 = 5.3620\,\mathrm{GHz}$) and $\nu_2 = 5.09791\,\mathrm{GHz}$ ($\nu_2 = 5.3637\,\mathrm{GHz}$), respectively (cf. vertical dashed lines in fig. 6), in the vicinity of the top edge of the TE PP gap displayed in fig. 1(c) (fig. 1(d)).

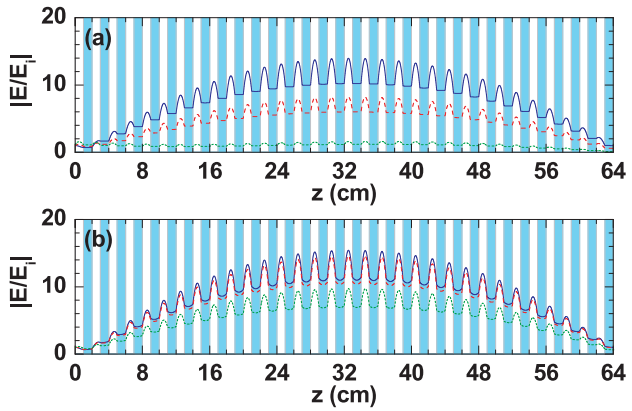

Fig. 8: (Color online) PP-gap soliton for (a) $\theta = \pi/24$ and (b) $\theta = \pi/6$. Solid, dashed and dotted lines correspond to $\gamma = 0$, $\gamma = 10^{-5}\,\mathrm{GHz}$ and $\gamma = 10^{-4}\,\mathrm{GHz}$, respectively. Results for each value of γ were obtained for the value of $-\alpha|E_i|^2$ corresponding to the local maximum of the transmission coefficient as a function of the defocusing nonlinearity power at (a) $\nu = 5.09791\,\mathrm{GHz}$ and (b) $\nu = 5.3637\,\mathrm{GHz}$ (cf. fig. 7 and tables 3 and 4).

plasmon mode is very weak and the transmission feature associated with the one-soliton excitation is quite feeble so that the corresponding result in fig. 8(a) is hardly noticeable.

To conclude, we have presented a thorough study of the absorption effects on the PP-gap soliton-induced transparency in 1D Kerr/metamaterial superlattices. Although calculations are presented in the TE configuration, similar results (not shown here) are also straightforwardly obtained in the TM configuration. As detailed in previous work for normal-material/metamaterial superlattices [6,7],

Table 3: Peak position ($-\alpha|E_i|^2$) of the TE transmission coefficient as a function of the defocusing nonlinearity power. Results were obtained for three different values of the damping constant γ, $\theta = \pi/24$, and $\nu = 5.09791\,\mathrm{GHz}$ in the vicinity of the top edge of the TE PP gap depicted in fig. 1(c).

γ (GHz)	Peak position
0	6.5899×10^{-5}
10^{-5}	1.8898×10^{-4}
10^{-4}	0.0033

Table 4: Peak position ($-\alpha|E_i|^2$) of the TE transmission coefficient as a function of the defocusing nonlinearity power. Results were obtained for three different values of the damping constant γ, $\theta = \pi/6$, and $\nu = 5.3637\,\mathrm{GHz}$ in the vicinity of the top edge of the TE PP gap depicted in fig. 1(d).

γ (GHz)	Peak position
0	4.1469×10^{-5}
10^{-5}	4.6434×10^{-5}
10^{-4}	1.0365×10^{-4}

for oblique incidence, the PP gap results from resonant PP waves excited by the coupling of the electric (or magnetic) bulk-like longitudinal plasmon modes with the incident eletromagnetic field, *i.e.*, the PP waves are excited by the magnetic field, in the TE case, or driven by the electric field, in the TM case. Results indicate that, by substituting the nondispersive linear layer by a nonlinear Kerr layer, one obtains that, for frequencies close to the bottom or top edge of the PP gap, the transmission of a finite Kerr/metamaterial superlattice presents a multistable behavior. The transmission switches from very low values to the maximum transparency at particular values of the incident power even in the presence of loss effects. At these frequencies around the edges of the PP gap and for those singular points where transmission becomes maximum, results suggest the existence of localized PP-gap solitons of various orders depending on the particular value of the incident power. Moreover, by controlling the angle of the incident eletromagnetic field together with nonlinearity strength, one may overcome absorption effects and realize resonant excitation of one-soliton, two-soliton, ..., PP-gap solutions in 1D Kerr/metamaterial superlattices. We have also calculated transmission in the self-focusing regime and preliminary results indicate that, at the particular frequency region studied here, one must significantly increase the nonlinear strength to induce transparency. Nonetheless, although work on the self-focusing regime is still in progress, we do believe one may find similar results to the ones reported here, but within a different range of the parameter space. The present results reveal, therefore, phenomena involving new PP-gap soliton-induced resonant solutions leading to the

transparency of a stack with nonlinear inclusions, a nonlinear optical analog of the electronic barrier-transmission resonances, and which may lead to potential applications in sensors and optical devices.

* * *

We would like to thank the Scientific Colombian Agency CODI - University of Antioquia and Brazilian Agencies CNPq and FAPESP (Proc. 2012/51691-0), for partial financial support.

REFERENCES

[1] Liu N., Guo H., Fu L., Kaiser S., Schweizer H. and Giessen H., *Nat. Mater.*, **7** (2008) 31.
[2] Xiao S., Drachev V. P., Kildishev A. V., Ni X., Chettiar U. K., Yuan H.-K. and Shalaev V. M., *Nature*, **466** (2010) 735.
[3] Zhang S., Fan W., Panoiu N. C., Malloy K. J., Osgood R. M. and Brueck S. R. J., *Phys. Rev. Lett.*, **95** (2005) 137404.
[4] Shalaev V. M., Cai W., Chettiar U. K., Yuan H.-K., Sarychev A. K., Drachev V. P. and Kildishev A. V., *Opt. Lett.*, **30** (2005) 3356.
[5] Kreibig U. and Vollmer M., in *Optical Properties of Metal Clusters* (Springer, Berlin) 1995.
[6] Reyes-Gómez E., Mogilevtsev D., Cavalcanti S. B., Carvalho C. A. A. and Oliveira L. E., *EPL*, **88** (2009) 24002.
[7] de Carvalho C. A. A., Cavalcanti S. B., Reyes-Gómez E. and Oliveira L. E., *Phys. Rev. B*, **83** (2011) 081408(R).
[8] Ye F., Mihalache D., Hu B. and Panoiu N. C., *Phys. Rev. Lett.*, **104** (2010) 106802.
[9] Kou Y., Ye F. and Chen X., *Opt. Lett.*, **37** (2012) 3822.
[10] Kou Y., Ye F. and Chen X., *Opt. Lett.*, **38** (2013) 1271.
[11] Chen W. and Mills D. L., *Phys. Rev. Lett.*, **58** (1987) 160.
[12] Chen W. and Mills D. L., *Phys. Rev. B*, **36** (1987) 6269.
[13] Hedge R. S. and Winful H. G., *Microwave Opt. Technol. Lett.*, **46** (2005) 528.
[14] Hedge R. S. and Winful H. G., *Opt. Lett.*, **30** (2005) 1852.
[15] Cavalcanti S. B., Brandão P. A., Bruno-Alfonso A. and Oliveira L. E., *Opt. Lett.*, **39** (2014) 178.
[16] Zhou J., Koschny T. and Soukoulis C. M., *Opt. Express*, **16** (2008) 11147.
[17] Plum E., Fedotov V. A., Kuo P., Tsai D. P. and Zheludev N. I., *Opt. Express*, **17** (2009) 8548.
[18] Gupta S. D., *J. Opt. Soc. Am. B*, **6** (1989) 1927.
[19] Peschel T., Dannberg P., Langbein U. and Lederer F., *J. Opt. Soc. Am. B*, **5** (1988) 29.
[20] Trutschel U. and Lederer F., *J. Opt. Soc. Am. B*, **5** (1988) 2530.